

# Fast X-ray Imaging Beamline at SSRF

Ke Li<sup>1</sup>, Hong-Lan Xie<sup>\*1</sup>, Ya-Nan Fu<sup>1</sup>, Fei-Xiang Wang<sup>1</sup>, Guo-Hao Du<sup>1</sup>, Jian-Feng Ji<sup>1</sup>, Biao Deng<sup>1</sup>, Ti-Qiao Xiao<sup>1</sup>

<sup>1</sup>Shanghai Synchrotron Radiation Facility, Shanghai Advanced Research Institute, Chinese Academy of Sciences, Shanghai, 201204, China

\*Correspondence e-mail: xiehl@sari.ac.cn

## Abstract:

The fast X-ray imaging beamline (BL16U2) at Shanghai Synchrotron Radiation Facility (SSRF) is a new beamline that provides X-ray micro-imaging capabilities across a wide range of time scales, spanning from 100 ps to  $\mu$ s and ms. This beamline has been specifically designed to facilitate the investigation of a wide range of rapid phenomena, such as the deformation and failure of materials subjected to intense dynamic loads. In addition, it enables the study of high-pressure and high-speed fuel spray processes in automotive engines. The light source of this beamline is a cryogenic permanent magnet undulator (CPMU) that is cooled by liquid nitrogen. This CPMU can generate X-ray photons within an energy range of 8.7-30 keV. The beamline offers two modes of operation: monochromatic beam mode with a liquid nitrogen-cooled double-crystal monochromator (DCM) and pink beam mode with the first crystal of the DCM out of the beam path. Four X-ray imaging methods were implemented in BL16U2: single-pulse ultrafast X-ray imaging, microsecond-resolved X-ray dynamic imaging, millisecond-resolved X-ray dynamic micro-CT, and high-resolution quantitative micro-CT. Furthermore, BL16U2 is equipped with various in situ impact loading systems, such as a split Hopkinson bar system, light gas gun, and fuel spray chamber. Following the completion of the final commissioning in 2021 and subsequent trial operations in 2022, the beamline has been officially available to users from 2023.

**Keywords:** multiple time-scale X-ray imaging, single-pulse X-ray imaging, dynamic 2D imaging, dynamic micro-CT.

## 1 Introduction:

With physical and chemical mechanisms being explored in depth, researchers increasingly demand higher spatial and temporal resolutions for in situ imaging experiments. These experiments include studying the deformations and failures of materials under strong dynamic loads<sup>[1-4]</sup>, as well as the high-pressure and high-speed spray processes of fuel in automobile engines<sup>[5-7]</sup>. Current international X-ray imaging technology tends to have a higher spatial resolution (nanometer scale) and faster temporal resolution (milliseconds to hundreds of picoseconds). Fast X-ray imaging methods have been established for major third-generation synchrotron radiation sources such as 32ID<sup>[8]</sup>, 7ID<sup>[9]</sup>, 35ID-B<sup>[10]</sup>, and 2BM<sup>[11]</sup> at APS in the United States; ID19<sup>[12]</sup>, ID15a<sup>[13]</sup>, and ID10<sup>[14]</sup> at ESRF in Europe; and BL47XU<sup>[15]</sup> at SPring-8 in Japan. These methods offer imaging temporal resolutions ranging from milliseconds (ms), microseconds ( $\mu$ s), and nanoseconds (ns) to tens of picoseconds (ps). As one of the Phase-I beamlines at the Shanghai Synchrotron Radiation Facility (SSRF)<sup>[16-18]</sup>, the X-ray imaging and biomedical applications beamline (BL13W1) has developed many types of X-ray imaging methods<sup>[19-25]</sup>. However, owing to limitations of the insertion device and optical setup, it is difficult to achieve the required temporal resolution.

The construction of a Fast X-ray Imaging beamline (BL16U2), one of the SSRF Phase II project's beamlines, began in 2016. After five years of dedicated effort, it completed its final commissioning in 2021. This beamline aims to provide X-ray micro-imaging on multiple time scales, ranging from 100 ps to  $\mu$ s and ms. This allows for in-situ and real-time observation of various fast processes, addressing the most pressing needs of most users.

In this paper, we introduce the details of this beamline, including the optical and experimental setups, experimental methods developed for users, and key performance parameters.

## 2 Beamline

### 2.1 Light source

The X-ray source of BL16U2 was a 3.06 m long cryogenic permanent magnet undulator (CPMU) with a period length of 18 mm. The maximum magnetic field strength exceeds 0.93 T under liquid nitrogen cooling. With a total power of over 6.1 kW, this undulator source can emit over  $1 \times 10^{16}$  photons/s in the pink beam mode when the magnet gap is set to the minimum value of 6 mm. Detailed information on the BL16U2 beam is presented in **Table 1**. The photon energy spectrum measured using a scanning monochromator at the actual sample point when the current in the storage ring was 200 mA is shown in Fig. 1. The peak intensity at the low-energy end of the graph is reduced owing to absorption by air.

**Table 1** Specifications of BL16U2 beamline

Equipment	Specifications			
Light source	3.06 m long CPMU			
Periods	170			
Period length	18 mm			
Electron Energy	3.5 GeV			
Designed storage ring current	300 mA			
Maximum magnetic field strength	>0.93 T			
Maximum K value	1.563			
Total power	6117.5 W			
Magnet Gap	6-30 mm			
Energy range	8.7-30 keV			
First harmonic	2910-5100 eV			
Effective source size (FWHM)	$631.3 \times 20.5 \mu\text{m}^2$			
Source divergence (Gap = 6 mm)	$\sigma_x$	$\sigma_{x'}$	$\sigma_y$	$\sigma_{y'}$
	265.2 $\mu\text{m}$	20.2 $\mu\text{rad}$	8.75 $\mu\text{m}$	4.87 $\mu\text{rad}$
Brilliance @ 10 keV	$4.6 \times 10^{19}$ phs/s/mrad <sup>2</sup> /mm <sup>2</sup> /0.1%BW			

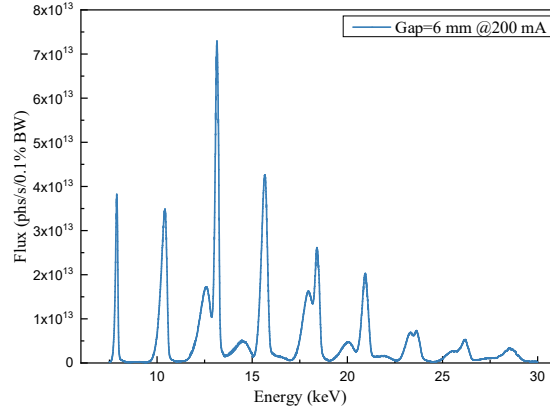


**Fig. 1** Photon energy spectrum measured at the actual sample point (Gap=6 mm).

## 2.2 Beamline optics

A schematic of the BL16U2 beamline is shown in Fig. 2. The optics hutch contained white-beam slits, a horizontal reflecting mirror, a double-crystal monochromator (DCM), and monochromatic beam slits. Three CVD diamond windows were used to maintain a high vacuum while withstanding the high thermal load of the pink CPMU beam. No additional optical units were used to maximize the photon flux from the light source.

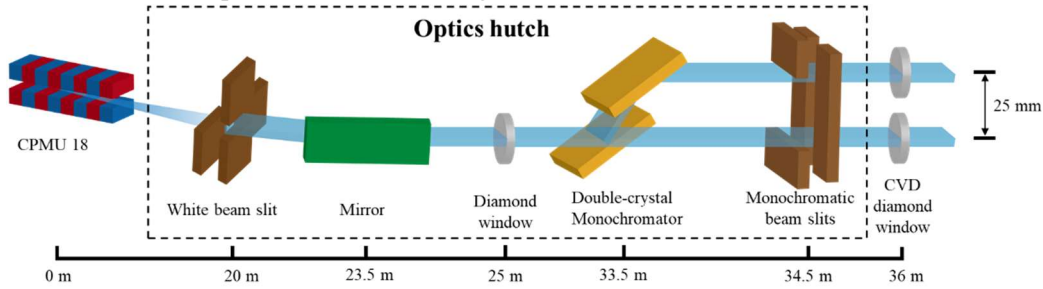


**Fig. 2** Schematic layout of BL16U2 optics hutch.

Given that the BL16U2 and BL16U1 beamlines share a 12 m long straight section of the storage ring, the inclusion of a horizontal deflecting mirror is necessary to enhance the angle between these two beamlines. The mirror was a plane crystal coated with platinum, and the grazing incidence angle was set to 2.5 milliradians (mrad) to ensure high reflectance across a broad range of energies.

Downstream, a DCM consisting of two Si (111) plane crystals is positioned at a distance of 33.5 m from the source point. Cooled by liquid nitrogen, the crystal pair can generate monochromatic photon beams ranging from 8.7-30 keV while maintaining an energy resolution ( $\Delta E/E$ ) of  $2 \times 10^{-4}$ . The first DCM crystal can lie horizontally and remain outside the path of the pink beam, allowing the direct transmission of the pink beam to the experimental hutch. Two operational modes of the beamline were achieved. The beam altitude of the pink light mode was 1300 mm, which increased to 1325 mm when switched to the monochromatic light mode. No focusing mirrors were present in the optical path, which resulted in a parallel beam entering the experimental hutch. The beam measured at the sample point was 2.6 mm (horizontal)  $\times$  1.8 mm (vertical).

## 2.3 Experimental station setup

**Fig. 3(a)** presents a schematic representation of the experimental station BL16U2, whereas **Fig.**

**3(b)** shows the actual layout of the station. The station can be divided into four sections from front to back: the beam monitor section, in situ 2D imaging section, dynamic CT section, and high-resolution CT section.

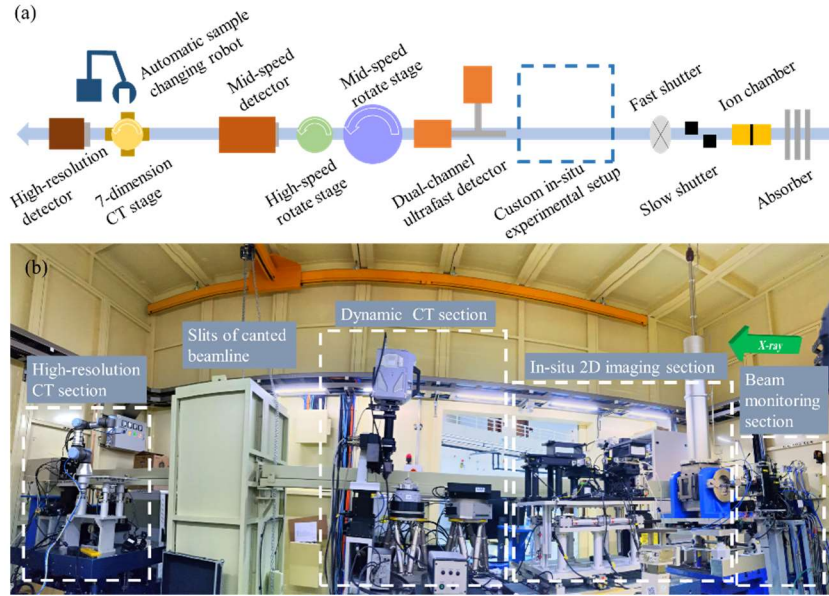


**Fig. 3** Experimental station set of BL16U2, (a) schematic diagram of experiment hutch, (b) actual picture of the experiment station setup.

The beam monitoring section comprises several components: a beam absorber, ion chamber, slow shutter, and fast shutter. The beam absorber was equipped with three water-cooled aluminum blocks (3 mm, 5 mm, and 10 mm thick) to protect detectors and sensitive samples from potential radiation damage caused by excessive light intensity. The primary purpose of the ion chamber is to monitor fluctuations in the light intensity of monochromatic light. Therefore, if the station operates in pink light mode, it will move out of the light path. The slow-shutter mechanism is cooled by water and is capable of vertical movement, allowing the creation of a time window of X-ray openings spanning several decades of milliseconds. In contrast, the fast shutter consisted of two rotary tungsten blocks, reducing the X-ray exposure time to less than 1 ms.

Downstream refers to a free space measuring 1.4 meters in length, specifically designated for users to install their own in situ experimental devices. A mobile optical table featuring an adjustable height range of 550–750 mm was presented. **Fig. 4** shows imaging detectors available on the BL16U2 beamline, which are the high-speed X-ray imaging detector with a Kirana camera (**Fig. 4(a)**), the ultra-fast X-ray imaging detector with two Andor Intensified Charge-coupled Device (ICCD) cameras (**Fig. 4(b)**), the fast X-ray imaging detector with a Photron camera (**Fig. 4(c)**), the mid-speed X-ray imaging detector with a pco.dimax HS4 camera (**Fig. 4(d)**) and the high-resolution X-ray detector with a HAMAMATSU camera (**Fig. 4(e)**).

A triple-lens dual-channel X-ray optical conversion system with high efficiency and a large numerical aperture (NA) was developed to fulfill the requirements for ultrafast X-ray detection. This system can provide magnifications of 5 $\times$ , 10 $\times$ , and 20 $\times$ , and the NA values are 0.3, 0.4, and 0.5. A mirror with half-transmission and half-reflection properties was used to divide the incident light into two beams for two separate ICCD cameras with 2 ns gate width for single pulse ultrafast X-ray imaging.

This configuration allows for an increased capture frequency in dynamic 2D imaging and the acquisition of two transient images in single-pulse ultrafast imaging. As depicted in **Fig. 4(a)** and **(b)**, the selection of cameras for this detector can vary depending on the purpose of the experiment. The available options include the Karana 5M camera (with a resolution of 30  $\mu\text{m}/\text{pixel}$  and 925 $\times$ 768 pixels) for high-speed X-ray imaging and the Andor iStar ICCD camera (with a resolution of 13  $\mu\text{m}/\text{pixel}$  and 1024 $\times$ 1024 pixels) for single pulse ultrafast X-ray imaging.



**Fig. 4** Imaging detectors available on BL16U2 beamline. (a) the high-speed X-ray imaging detector with a Kirana camera, (b) the ultra-fast X-ray imaging detector with two Andor ICCD cameras, (c) the fast X-ray imaging detector with a Photron camera, (d) the mid-speed X-ray imaging detector with a pco.dimax HS4 camera, (e) the high-resolution X-ray detector with a HAMAMATSU camera.

The dynamic CT section comprises two air-bearing rotation stages, RT-150s and RT-250s, from LAB and a ball-bearing rotation stage, RSML-100, from Coretech. The RT-250s can carry up to 25 kg of in situ devices and have a maximum rotation speed of 120 rpm. RT-150s can carry a relatively low axial load of 2 kg and have a high rotation speed of up to 800 rpm. Compared to the two air-bearing stages, the RSML-100 demonstrated superior performance in terms of axial load capacity and rotation speed, with the ability to handle loads of up to 7 kg and rotate at speeds of up to 1800 rpm. However, it exhibits a higher surface runout error, indicating a less precise surface alignment. Two imaging detectors are available to capture dynamic CT or 2D images that last a few seconds. The first was a large-NA single-lens fast-imaging detector at 4 $\times$  or 8 $\times$  magnification (**Fig. 4(c)**). The second detector was a triple-lens mid-speed imaging detector with 2 $\times$ , 5 $\times$ , and 8 $\times$  magnifications (**Fig. 4(d)**). Both detectors were developed by an X-ray imaging group at the SSRF [26, 27]. Alternative cameras include the Fastcam SA-Z, which has a resolution of 20  $\mu\text{m}/\text{pixel}$  and a pixel count of 1024 $\times$ 1024, and the pco.dimax HS4, which has a resolution of 11  $\mu\text{m}/\text{pixel}$  and a pixel count of 2000 $\times$ 2000.

A high-resolution CT section was designed to provide a batch operation of multiple high-resolution micro-CTs [28]. This section comprises a 7-dimensional CT stage from Kohzu, an automated sample-changing robot, and a high-resolution detector. Up to 40 samples can be placed on the pallet, allowing the robot to efficiently retrieve them, thereby enhancing the efficiency of the micro-CT experiments. The data-acquisition system employed in this study is shown in **Fig. 4(e)**. It comprises an X-ray optical conversion system provided by Optique Peter and a CMOS camera manufactured by HAMAMATSU. Specifically, the camera model used is the Flash 4.0 C11440, which has a pixel size of 6.5  $\mu\text{m}$  and a pixel count of 2048 $\times$ 2048. The optical conversion system offers magnifications of 2 $\times$ , 4 $\times$ , 10 $\times$ , and 20 $\times$ .

**Table 2** presents a comprehensive overview of the specifications of all X-ray imaging detectors available on BL16U2. This includes pixel size, field of view, maximum capture speed, and suitable experimental methods. The smaller value between the beam size and the effective imaging area of the detector constrains the field of view. Scintillators available in BL16U2 are LuAG: Ce (thickness:

100  $\mu\text{m}$  and 50  $\mu\text{m}$ , decay time: 70 ns) and CRY019 (thickness: 100  $\mu\text{m}$ , decay time: 42 ns) from CRYTUR Ltd, depending on different spatial resolution and demand of fluorescence relaxation time.

**Table 2** Specifications of X-ray imaging detectors on BL16U2

Type	Camera	Pixel size	Field of view	Max capture speed	Aims and scopes
High-resolution X-ray imaging detector	HAMAMATSU Flash 4.0	0.325 $\mu\text{m}$ 0.650 $\mu\text{m}$ 1.625 $\mu\text{m}$ 3.250 $\mu\text{m}$	0.6 mm (H) $\times$ 0.6 mm (V) 1.3 mm (H) $\times$ 1.3 mm (V) 2.6 mm (H) $\times$ 1.8 mm (V) 2.6 mm (H) $\times$ 1.8 mm (V)	200 fps	High-resolution CT
Mid-speed X-ray imaging detector	pco.dimax HS4	1.10 $\mu\text{m}$ 2.20 $\mu\text{m}$ 5.50 $\mu\text{m}$	2.2 mm (H) $\times$ 1.8 mm (V) 2.6 mm (H) $\times$ 1.8 mm (V) 2.6 mm (H) $\times$ 1.8 mm (V)	46746 fps	Dynamic CT; 2D imaging for process in seconds
Fast X-ray imaging detector	Photron fastcam SA-Z	2.50 $\mu\text{m}$ 5.00 $\mu\text{m}$	2.5 mm (H) $\times$ 1.8 mm (V) 2.6 mm (H) $\times$ 1.8 mm (V)	224000 fps	Dynamic CT; 2D imaging for process in tens of milliseconds
High-speed X-ray imaging detector	Kirana 5M	1.50 $\mu\text{m}$ 3.00 $\mu\text{m}$ 6.00 $\mu\text{m}$	1.3 mm (H) $\times$ 1.1 mm (V) 2.6 mm (H) $\times$ 1.8 mm (V) 2.6mm(H) $\times$ 1.8mm(V)	5M fps	2D imaging for process in milliseconds
Ultra-fast X-ray imaging detector	Two Andor ICCD	0.65 $\mu\text{m}$ 1.30 $\mu\text{m}$ 2.60 $\mu\text{m}$	0.6 mm (H) $\times$ 0.6 mm (V) 1.3 mm (H) $\times$ 1.3 mm (V) 2.6 mm (H) $\times$ 1.8 mm (V)	Gate time 2 ns, 2 frames at once	Single pulse ultra-fast imaging for process in microseconds

Furthermore, the BL16U2 is equipped with two sets of in situ impact loading systems designed explicitly for material science studies. The first system is a split Hopkinson bar system (**Fig. 5(a)**), which can apply tensile and compressive loads at strain rates ranging from  $10^2$  to  $10^4$  /s. Two rods with 6 mm and 12.7 mm diameters are available for different sample sizes and strain rates. The rods can be propelled by compressed air, nitrogen ( $\text{N}_2$ ), or helium (He) at a maximum gas pressure of 2 MPa. The second system, shown in **Fig. 5(b)**, is a vertical light-gas gun. This gun has a barrel length of 2.2 m and a caliber of 10 mm. Compressed air,  $\text{N}_2$ , or He at pressures ranging from 0 to 15 megapascals (MPa) propels the bullet through the barrel, achieving a maximum velocity of 1 kilometer per second (km/s) before impacting the target sample. Strain sensors and a timing synchronization system were prepared to acquire loading data and material failure images



simultaneously [29].

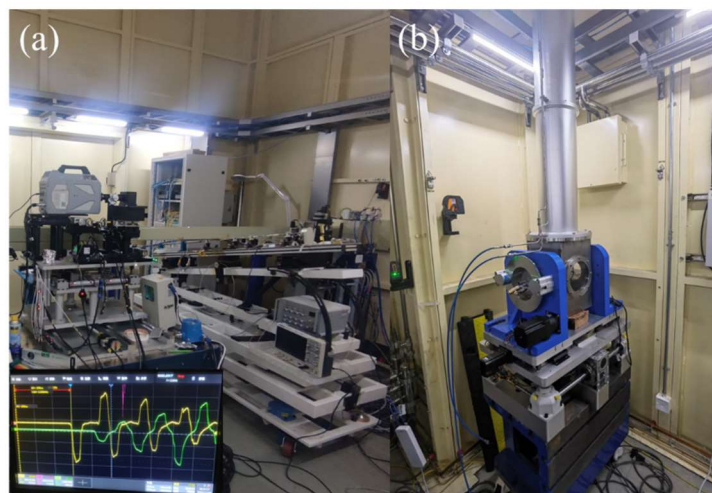


**Fig. 5** In-situ impact loading systems, (a) a split Hopkinson bar system, (b) a vertical light gas gun.

Our beamline is equipped with a specially designed spray chamber for researchers to investigate the high-pressure/speed spray process of fuel in automobile engines [30]. This chamber allowed for the observation of the injection nozzles and sprayed fuel through a window without any concerns regarding fuel vapor leakage (see **Fig. 6(a)**). Two types of common rail systems were prepared to simulate the engines of various technological routes. The first utilizes a variable-section piston in conjunction with a pneumatic booster pump to handle volatile, low-viscosity hydrocarbon fuels such as gasoline (see **Fig. 6(b)**). The pressure adjustment range was 5–50 MPa with minimal fluctuations of less than 5%. The second option accommodates high-viscosity, low-volatility hydrocarbon fuels such as diesel (**Fig. 6(c)**). The pressure adjustment range was 30–250 MPa with a pressure fluctuation of less than 5%.

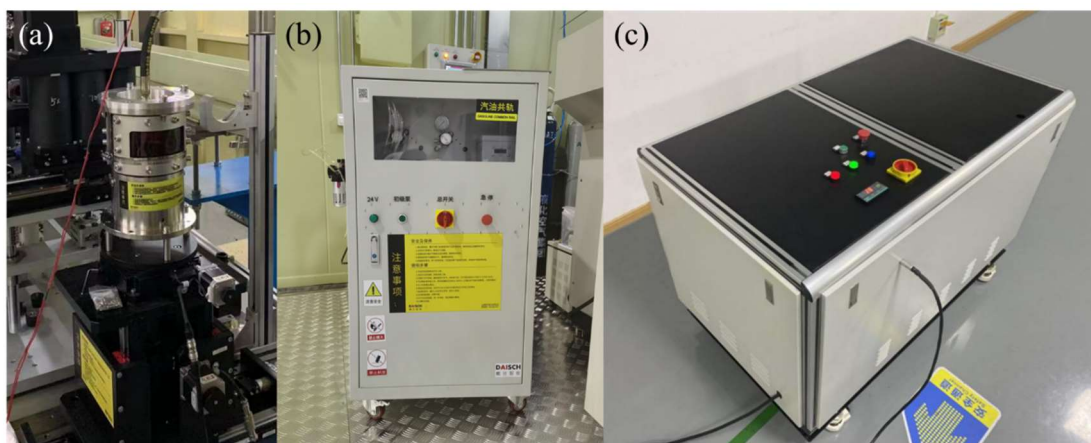


**Fig. 6** In-situ fuel spray systems, (a) a spray chamber, (b) low-pressure common rail system for gasoline, (c) high-pressure common rail system for diesel.

## 2.4 Beamline control and data acquisition

The beamline control section was located at the rear of the experimental hutch. The status of the entire beamline was continuously monitored, and all equipment located in the optical and experimental hutches was remotely adjusted within this section. To facilitate the integration of

different detectors, sample stages, and in situ loading devices, data-acquisition software was developed, as depicted in **Fig. 7**. The left section of the software interface is dedicated to the detector setup, encompassing essential parameters for capturing, such as frame rate, shutter speed, and pixel resolution. The variability of this aspect is contingent upon the choice of detector made by users. The central part of the software includes real-time displays of the detectors. The contrast and brightness of a preview image can be adjusted by manipulating the upper and lower thresholds of the histogram. Several supporting functions are available for the buttons on the interface's right side. These functions include the setup of the sample-changing robot, timing of the shutter trigger, filter system, and various CT scan modes. The control of the sample stage motion is subordinate to the supporting functions, enabling users to freely manipulate the positions of the samples or the in situ loading devices. Similar to the detector configuration, this component can be modified when transitioning to the alternative sample stages.

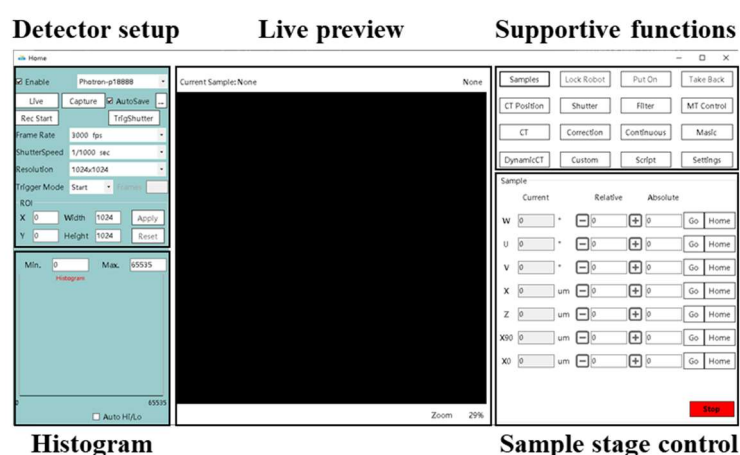


**Fig. 7** The interface of the image acquisition and motion control software developed by X-ray imaging group at SSRF.

### 3 Experimental methods

Several X-ray imaging methods have been established for the BL16U2, encompassing temporal scales ranging from 100 ps to milliseconds. These methods offer spatial resolution at the micrometer scale, including single-pulse ultrafast X-ray imaging, microsecond-resolved X-ray dynamic imaging, millisecond-resolved X-ray dynamic micro-CT, and high-resolution quantitative micro-CT.

#### 3.1 single-pulse ultrafast X-ray imaging

Traditional X-ray imaging utilizes fast cameras with short gate times to prevent motion blurring of the target<sup>[31]</sup>. However, the minimum gate time of existing commercial fast cameras ranges from 2 to 3 ns to more than 100 ns<sup>[32]</sup>. For a transient loading process with a velocity exceeding 1 km/s, even the shortest gate time results in motion blur ranging from tens to hundreds of micrometers, leading to a significant degradation in spatial resolution. By contrast, single-pulse ultrafast X-ray imaging replaces the gate time of cameras with the temporal duration of the electron bunch in a storage ring as the exposure time for capturing an image<sup>[33]</sup>.

A validation experiment was conducted as a part of the beamline commissioning process. This experiment used single-pulse ultrafast X-ray imaging to observe the formation of cavities in water induced by a nanosecond-pulsed laser. First, the implementation of single-pulse ultrafast X-ray



imaging requires the operation of a storage ring in a specialized mode, known as the hybrid mode. As shown in **Fig. 8(a)**, the storage ring contains a large number of electrons along with a sequence of small bunches. The duration required for each bucket to complete the full revolution in the storage ring was 1.44  $\mu\text{s}$ . Additionally, no bunches were present in the region 200 ns before or after the large bunch, which had a duration of only 60 ps. Therefore, in theory, during a period of up to 400 ns, only the central 60 ps is utilized for image exposure. Considering that the fluorescence relaxation time of the LuAG: Ce scintillator was 70 ns, which is much shorter than 200 ns, we can assume that a single pulse generated the acquired images. The experimental configuration used for the BL16U2 is shown in **Fig. 8(b)**. An ultrafast X-ray imaging detector with two ICCDs was used in this experiment, as shown in **Table 2**. A 1064 nm-wavelength nanosecond laser beam was focused on a point in water to generate a scorching spot, and a cavity occurred due to ultra-fast evaporation. The generation and rupture processes typically last for a few microseconds. A logical timing diagram for each key component is shown in **Fig. 8(c)**. Precise synchronization of the detector and the synchrotron source was realized by adjusting the time delay  $\Delta t_1$  between the ICCD trigger and the RF signal of the storage ring and comparing the brightness of captured images at different time delays. Owing to the highly repeatable laser loading, we can achieve the evolution of cavity morphology at various stages by systematically manipulating the time delay  $\Delta t_2$  of the laser prior to the emission of a single pulse. The results are presented in **Fig. 8(d)-(f)**. As shown, a liquid jet was generated from the rupture of the bubble and rapidly penetrated the entire bubble at a speed of over 100 m/s. Owing to the high temporal resolution of single-pulse ultrafast X-ray imaging, no motion blurring was observed during this fast process.

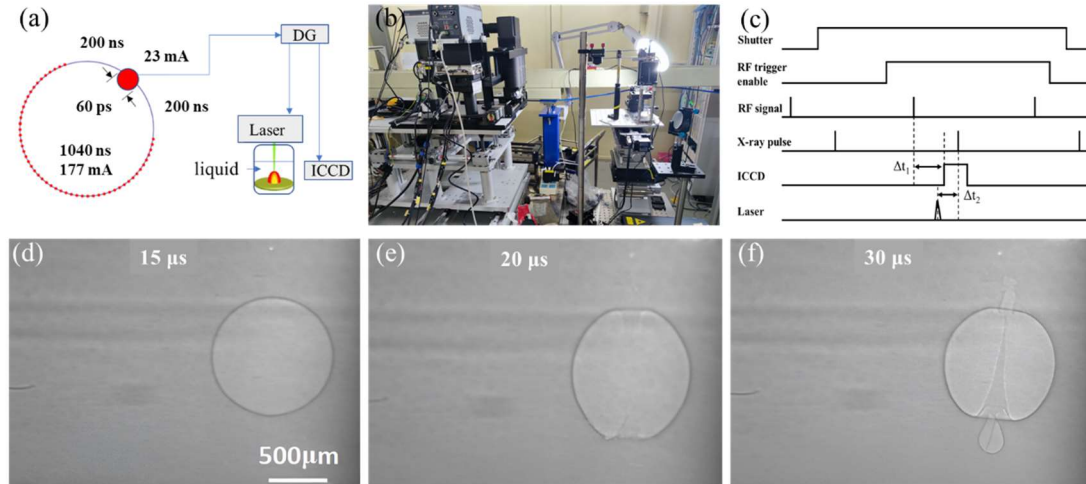


**Fig. 8** single-pulse ultrafast X-ray imaging, (a) diagram of the experiment, (b) experimental setup, (c) a logical timing diagram for each key component, (d)-(f) bubble rupture and the generation of liquid jet captured using different  $\Delta t_2$ .

In addition, our experimental setup included a dual-channel ultrafast detector equipped with two intensified charge-coupled devices (ICCDs). This configuration allowed us to capture two transient single-pulse images of the same incident by introducing a specific time delay between the two ICCDs. The time delay must be a multiple of 1.44  $\mu\text{s}$ . As an illustrative example, eight transient single-pulse images were acquired during four laser loadings; the corresponding results are shown in **Fig. 9**. The time delays of the first ICCD after the laser loading are 5, 20, 30, and 50  $\mu\text{s}$ . Subsequently, the second ICCD is set to trigger 1.44  $\mu\text{s}$  or 14.4  $\mu\text{s}$  after the first ICCD. Once the images are arranged chronologically, the procedure for the microbubble expansion to rupture can

be recorded. The variation in the bubble diameter over time is shown in **Fig. 9(i)**, where the entire process can be divided into three parts: expansion, sustainability, and rupture. Each of these three parts lasted about 20  $\mu\text{s}$  each. It is important to note that the laser loading in this experiment exhibits high repeatability. However, in cases where an incident cannot be replicated, the current limitation allows for recording only two transient images in a single shot.

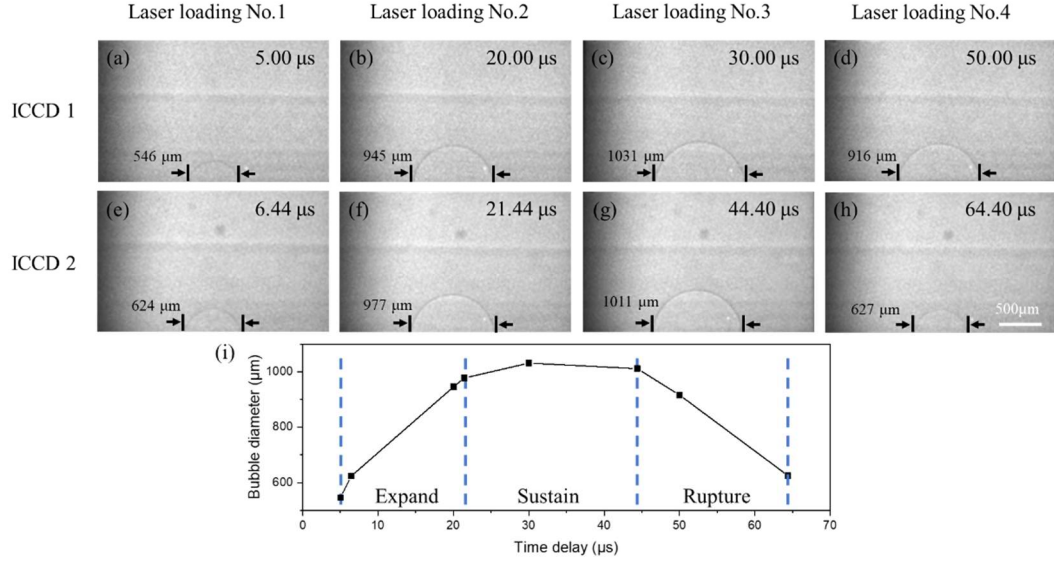


**Fig. 9** double transient single-pulse imaging during 4 laser loadings, (a)-(d) are captured by the first ICCD, (e)-(h) are captured by the second ICCD, (i) plot of bubble diameter over time.

### 3.2 Microsecond resolved X-ray dynamic imaging

X-ray 2D dynamic imaging is widely recognized as one of this field's most prevalent imaging techniques. Thanks to the increased photon flux and improved detector conversion efficiency, the BL16U2 can capture a continuous series of images with a temporal resolution of 2  $\mu\text{s}$  while maintaining a micrometer scale spatial resolution. The experimental setup was very similar to the single-pulse X-ray imaging experiment in **Fig. 8** and **9**, except that one of the ICCD of the dual-channel ultrafast X-ray imaging detector was substituted with the Kirana 5M fast camera, as depicted in **Fig. 10(a)** and **(b)**. The Kirana camera was set to external trigger mode in this experiment and synchronized with the laser loading. The frame rate was configured at 500,000 frames per second (fps) to achieve a favorable signal-to-noise ratio. This camera can capture images at a high frame rate while maintaining a large pixel array of  $924 \times 768$  pixels and a 10-bit image depth. The optical magnification of the detector has been chosen to be  $10\times$ , resulting in an equivalent pixel size of 3  $\mu\text{m}$ . A total of 180 images were recorded. The process of bubble rupture was depicted in **Fig. 10(c)-(f)**, acquired at times of 0  $\mu\text{s}$ , 2  $\mu\text{s}$ , 10  $\mu\text{s}$ , and 16  $\mu\text{s}$ , where 0  $\mu\text{s}$  refers to the start of the liquid jet generation. The generation of a liquid jet is observed. Additionally, the high spatial resolution enabled clear visibility of the wrinkles present on the conical surface of the jet.

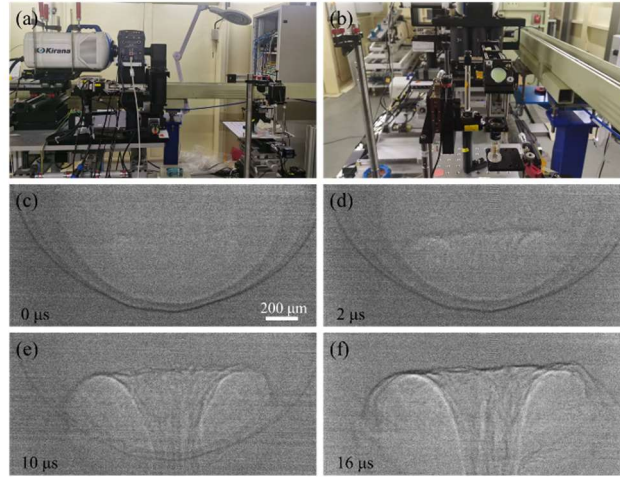


**Fig. 10** Microsecond resolved X-ray dynamic imaging, (a) and (b) experimental setup, (c)-(f) images captured at the moment of 0  $\mu$ s, 2  $\mu$ s, 10  $\mu$ s, and 16  $\mu$ s

### 3.3 millisecond resolved X-ray dynamic micro-CT

Dynamic micro-CT enables the acquisition of temporal changes in the three-dimensional spatial structure, making it an ideal tool for conducting in situ investigations into the mechanisms of system evolution. Dynamic micro-CT requires the acquisition of numerous sets of CT data within a single second, with each set comprising hundreds of projections. In addition, it is imperative to minimize the exposure time for each projection to mitigate motion blurring resulting from sample rotation. Therefore, the utilization of dynamic microscopy CT necessitates the availability of high photon fluxes emanating from the light source. Beamlines that utilize a bending magnet or wiggler source often require a pink beam to address deficiencies in the photon flux. However, the utilization of pink X-rays results in increased radiation damage to samples and reduced density resolution compared to monochromatic X-rays. The CPMU light source of the BL16U2 beamline exhibited a significantly high pink beam flux, which allowed for efficient flux even after monochromatization by DCM. This process maintains a good monochromaticity level of  $2 \times 10^{-4}$ . **Fig. 11 (a)** shows a validation experiment using a fast-foaming polyurethane material system with a monochromatic beam of 15 keV and an effective pixel size of  $2.2 \mu\text{m}$ .<sup>[34]</sup> As shown in **Fig. 7(b)-(g)**, the same slice (400th slice) of the reconstructed slices at different moments was selected for comparison. It can be observed that the bubbles in the slices change with time. From **(b)** to **(g)**, bubble in the red circle starts to shrink slowly from moment 0, then begins to accelerate from 0.3 s onwards, and finally disappears in the slice at 1.1 s. This indicates that the bubble was located in the 400th slice in the early stage and eventually left because of motion and volume changes. The minimum time interval between CTs is 50 ms, proving that the imaging system's dynamic CT time resolution reaches 50 ms. As a comparison, the highest reported temporal resolution is 75 ms with an effective pixel size of  $5 \mu\text{m}$  in the field of monochromatic X-ray dynamic micro-CT<sup>[35]</sup>.

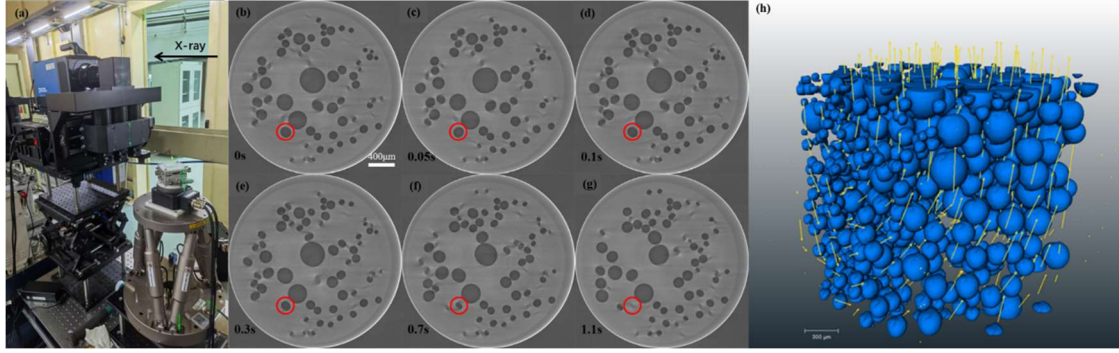


**Fig. 11** Millisecond resolved X-ray dynamic micro-CT, (a) experimental setup, (b)-(g) the slices at the time of 0 s, 0.05 s, 0.1 s, 0.3 s, 0.7 s, 1.1 s, (h) three-dimensional motion vector field of bubbles obtained by DVC analysis.

### 3.3 high-resolution quantitative micro-CT

Owing to the exceptional monochromaticity of DCM, it is possible to perform conventional in-line high-resolution quantitative micro-CT on BL16U2 [36, 37]. The detector has effective pixel sizes of 3.25  $\mu\text{m}$ , 1.625  $\mu\text{m}$ , 0.65  $\mu\text{m}$ , and 0.325  $\mu\text{m}$ , which correspond to different optical lenses.

A spatial resolution test of the system is presented in **Fig. 12** below, utilizing the JIMA RC-02b test card as a reference sample. The detector has an effective pixel size of 0.325  $\mu\text{m}$ , and the photon energy is 10 keV. It is possible to easily separate line groups with a width of 0.7  $\mu\text{m}$  from each other. The horizontal and vertical profiles depicted in **Fig. 12(b)** further demonstrate the high-quality imaging of the fine details at a scale of 0.7  $\mu\text{m}$ . In addition, the MTF values calculated using 0.8, 0.7, and 0.6  $\mu\text{m}$  line groups are 0.016, 0.014, and 0.006. As we can see, the MTF value of 0.6  $\mu\text{m}$  reduced significantly compared to 0.7 and 0.8  $\mu\text{m}$ , indicating that the highest spatial resolution is 0.7  $\mu\text{m}$ .

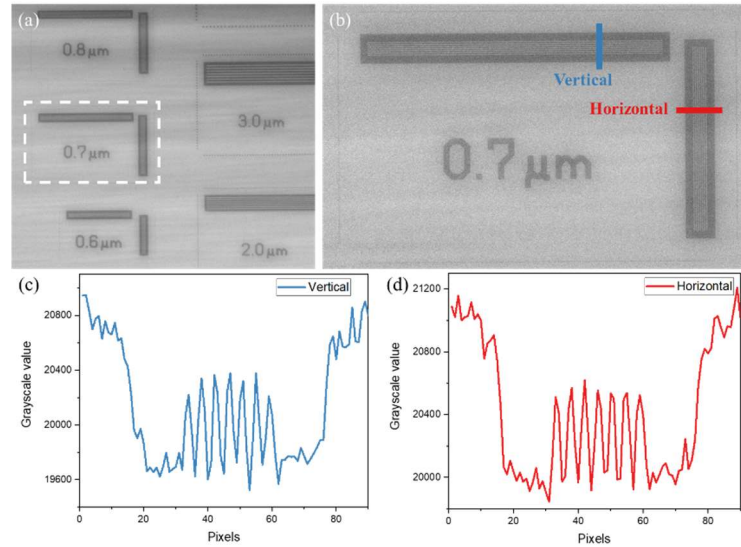


**Fig. 12** Spatial resolution test of the micro-CT system, (a) imaging of the JIMA RC-02b test card (pixel size 0.325  $\mu\text{m}$ ), (b) zoomed-in view of the white dashed square in (a), (c) and (d) vertical and horizontal line profiles of 0.7  $\mu\text{m}$ -width line groups.

An example of this system is shown in **Fig. 13**. this research focuses on a densely distributed C/C composite reinforced with fibers. In this composite, the diameter of carbon fibers is about 7  $\mu\text{m}$ ,



and the space between fibers is even smaller. Therefore, this composite simultaneously requires high spatial and density resolutions [36]. It is evident from the observations that carbon fibers can be extracted from the graphite matrix despite their proximity to each other. The orientation and tortuosity statistics of the 502 fibers extracted from a section are shown in **Fig. 13**. First, the polar angle  $\theta$  reflects the deviation of the fibers from the load direction. According to the data in **Fig. 13(b)**, 89.4% of the fibers were concentrated within a range of  $1.5^\circ$ , highlighting the consistency and excellent mechanical strength of the composite in the load direction. Based on the spatial distribution of the fibers in **Fig. 13(a)**, fibers with larger  $\theta$  values are scattered, while those with smaller  $\theta$  values are associated with high density. This demonstrates that the high consistency of the fibers reduced the pores and bulk graphite, thereby increasing the mechanical strength of the composite. The azimuthal angle  $\phi$  is another critical parameter for distinguishing aggregations in a bundle of fibers. As depicted in **Fig. 13(c)**, a sandwich structure is evident due to  $\phi$  differences, with interlayer boundaries marked by the white dashed line. In addition, the histogram in **Fig. 13(d)** shows that the  $\phi$  values of the two outer layers are around  $245^\circ$ , whereas that of the inner layer gradually changes from  $70^\circ$  to  $112^\circ$ . This indicates a fine degree of parallelism for the fibers of the same layer, in contrast to those of different layers.

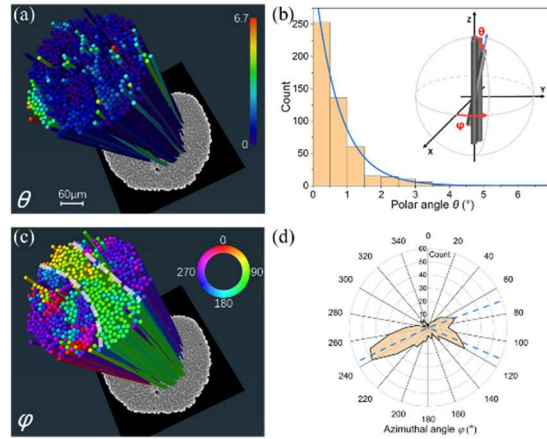


**Fig. 13** Images and plots for the statistical analyses of fibers in the C/C composite, (a) and (b) the spatial distribution and histogram for the polar angle  $\theta$  of each fiber, (c) and (d) the spatial distribution and histogram of the azimuthal angle  $\phi$  of each fiber.

#### 4 Final commissioning results

The BL16U2 beamline has completed its final commissioning phase and is now available for public use in experimental research. The test results for the key beamline parameters are listed in **Table. 3** below. All experimental results were obtained using a storage ring current of 200 mA and subsequently adjusted to reflect the data at 300 mA through proportional conversion. All specifications can be directly measured except for the photon flux of pink light and a single pulse. This is because the total flux has surpassed the current upper limit of energy-resolving photon-counting detectors. After deliberation with experts, a solution encompassing the entire spectrum of CPMU was deemed acceptable.

The following section provides a comprehensive breakdown of the steps involved. First, a monochromator was utilized to scan the CPMU spectrum, specifically targeting the energy range spanning the 3<sup>rd</sup> to 11<sup>th</sup> harmonics. Subsequently, the current in the ion chamber was meticulously recorded. The monochromatic photon flux at each recorded point in the initial step was then

calculated. Subsequently, the reflection rate, bandwidth of the double crystal, and absorption of the 1.5 m long air in the experimental hutch were considered in the calculations for each energy to determine the flux when the monochromator was not in line. Finally, the flux spectrum of the CPMU was plotted, as shown in **Fig. 1**. The total pink light flux can then be calculated using a simple integral.

Given that the current intensity of the electron bunches is directly correlated to the number of photons generated, we can use the flux of pink light at 200 mA and the current of the large bunch at 23 mA to calculate the photon number of single-pulse X-rays per second using proportionality. The repetition time of a single-pulse X-ray is 1.44  $\mu$ s, indicating that approximately 694,444 single pulses occur within one second. The numbers of photons in a single pulse are listed in **Table 3**.

**Table 3** Test results of BL16U2 beamline

Specifications	Design goals	Test results
Energy range	8.7-30 keV	8.3-30.5 keV
Energy resolution (measured with a Si 555 crystal analyzer)	$2 \times 10^{-4}$ @10 keV	$1.60 \times 10^{-4}$ @10 keV
Beam size at sample position (pink and monochromatic beam)	$1.5 \times 1.0$ mm <sup>2</sup>	$2.64 \times 1.87$ mm <sup>2</sup>
Photon flux	$1 \times 10^{13}$ phs/s @10 keV @300mA	$2.39 \times 10^{13}$ phs/s @10 keV @300mA
	$5 \times 10^{15}$ phs/s (pink light) @300mA	$1.31 \times 10^{16}$ phs/s (pink light) @300mA
	$1 \times 10^9$ phs (single pulse) @300mA	$1.5 \times 10^9$ phs (single pulse) @300mA
Temporal resolution of single-pulse ultrafast X-ray imaging	80 ps	60 ps
Spatial resolution	1 $\mu$ m	0.7 $\mu$ m
Temporal resolution of X-ray dynamic imaging	10 $\mu$ s	2 $\mu$ s
Temporal resolution of X-ray dynamic micro-CT	100 ms	50 ms

The results indicated that the measured values of the fast X-ray imaging beamline satisfied and exceeded the designed specifications.

## 5 Summary and conclusion

The X-ray fast imaging beamline at SSRF is a new beamline that can provide X-ray micro-imaging at various time scales, ranging from 100 ps to  $\mu$ s and ms. This beamline is specifically



designed to investigate rapid processes, including material deformations and failures under intense dynamic loads, as well as fuel's high-pressure and high-speed spray processes in automotive engines. A cryogenic permanent magnet undulator (CPMU) cooled by liquid nitrogen was chosen as the light source to generate X-ray photons within an energy range of 8.7-30 keV. The beamline offers two operational modes: pink and monochromatic. This was made possible using a liquid-nitrogen-cooled double-crystal monochromator. A variety of imaging detectors are currently available, offering spatial resolutions ranging from submicrometers to a few micrometers and temporal capabilities ranging from 100 ps to milliseconds. Furthermore, BL16U2 is equipped with various in situ impact loading systems, such as a split Hopkinson bar system, a vertical light gas gun, and a high-pressure/speed fuel spray chamber. Four X-ray imaging methods have been implemented in BL16U2, encompassing 60 ps single-pulse ultrafast X-ray imaging, 2  $\mu$ s time-resolved X-ray dynamic imaging, 50 ms time-resolved monochromatic X-ray dynamic micro-CT, and 0.325  $\mu$ m/pixel quantitative micro-CT. The results obtained from the final commissioning demonstrated that all the measured specifications not only met but also exceeded the design values. Consequently, the fast X-ray imaging beamline is now fully prepared to accommodate users from all over the globe.

**Conflict of interests:**

The authors claim no conflicts of interest.

**Author contributions:**

All authors contributed to the study conception and design. Material preparation was performed by Ke Li, Fei-Xiang Wang. Data collection and analysis were performed by Jian-Feng Ji, Ya-Nan Fu, Guo-Hao Du and Biao Deng. The first draft of the manuscript was written by Ke Li, Hong-Lan Xie and Ti-Qiao Xiao. All authors commented on previous versions of the manuscript. All authors read and approved the final manuscript.

**Fundings:**

This work was supported by the National Major Scientific Instruments and Equipment Development Project of China (Grant No. 11627901), the CAS Project for Young Scientists in Basic Research (YSBR-096), the National Key Research and Development Program of China (2021YFF0701202, 2021YFA1600703), and the National Natural Science Foundation of China (No. U1932205, 12275343).

**Acknowledgements:**

The authors are grateful to all colleagues of the imaging group at the SSRF for their kind help during construction and commissioning. The authors also thank their colleagues in the beamline engineering group and the storage ring operating group.

**Data Availability Statement:**

The data that support the findings of this study are openly available in Science Data Bank at <https://cstr.cn/31253.11.sciencedb.j00186.00175> and <https://www.doi.org/10.57760/sciencedb.j00186.00175>.

## References:

- [1] M.Z. Mo, M.X. Tang, Z.J. Chen, et al. Ultrafast visualization of incipient plasticity in dynamically compressed matter. *Nat. Commun.* **13**, 1055 (2022). <https://doi.org/10.1038/s41467-022-28684-z>
- [2] Y.Y. Zhang, S. Chen, Y. Cai, et al. Novel X-ray and optical diagnostics for studying energetic materials: a review. *Engineering* **6**, 992-1005 (2020). <https://doi.org/10.1016/j.eng.2020.06.019>
- [3] M.P. Olbinado, V. Cantelli, O. Mathon, et al. Ultra high-speed x-ray imaging of laser-driven shock compression using synchrotron light. *J. Phys. D: Appl. Phys.* **51**, 055601 (2018). doi: 10.1088/1361-6463/aaa2f2
- [4] S. Chen, Q.Y. Hou, Q.N. Wang, et al. Progress on Synchrotron Based in-Situ Dynamic X-Ray Diagnostics and Its Applications. *Chinese Journal of High Pressure Physics* **37**, 050104-050101-050104-050121 (2023). doi: 10.11858/gywlxb.20230747
- [5] Z.J. Wu, W.B. Zhao, Z.L. Li, et al. A review of engine fuel injection studies using synchrotron radiation x-ray imaging. *Automotive Innovation* **2**, 79-92 (2019). <https://doi.org/10.1007/s42154-019-00056-2>
- [6] A.G. Macphee, M.W. Tate, C.F. Powell, et al. X-ray imaging of shock waves generated by high-pressure fuel sprays. *Science* **295**, 1261-1263 (2002). doi: 10.1126/science.1068149
- [7] W.D. Huang, S. Moon, K. Ohsawa. Near-nozzle dynamics of diesel spray under varied needle lifts and its prediction using analytical model. *Fuel* **180**, 292-300 (2016). <https://doi.org/10.1016/j.fuel.2016.04.042>
- [8] C. Campbell, X. Tang, Y. Sechrest, et al. Ultrafast x-ray imaging of pulsed plasmas in water. *Physical Review Research* **3**, L022021 (2021). <https://doi.org/10.1103/PhysRevResearch.3.L022021>
- [9] D. Mamaikin, T. Knorsch, P. Rogler, et al. The effect of transient needle lift on the internal flow and near-nozzle spray characteristics for modern GDI systems investigated by high-speed X-ray imaging. *Int. J. Engine Res.* **23**, 300-318 (2022). <https://doi.org/10.1177/1468087420986751>
- [10] D. Capatina, K. D'amico, J. Nudell, et al. DCS-A high flux beamline for time resolved dynamic compression science—Design highlights, proceedings of the AIP Conference Proceedings. (AIP Publishing, 2016). <https://doi.org/10.1063/1.4952859>
- [11] V. Nikitin, A. Tekawade, A. Duchkov, et al. Real-time streaming tomographic reconstruction with on-demand data capturing and 3D zooming to regions of interest. *J. Synchrotron Radiat.* **29**, 816-828 (2022). <https://doi.org/10.1107/S1600577522003095>
- [12] B. Zielinski, T. Sadat, B. Lukić, et al. Characterization of local mechanical properties of Al/Cu Magnetic Pulse Welded joints under high strain rates using synchrotron X-ray imaging. *Mater. Lett.* **337**, 133943 (2023). <https://doi.org/10.1016/j.matlet.2023.133943>
- [13] G.B. Vaughan, R. Baker, R. Barret, et al. ID15A at the ESRF—a beamline for high speed operando X-ray diffraction, diffraction tomography and total scattering. *J. Synchrotron Radiat.* **27**, 515-528 (2020). <https://doi.org/10.1107/S1600577519016813>
- [14] Y. Chushkin, F. Zontone, E. Lima, et al. Three-dimensional coherent diffractive imaging on non-periodic specimens at the ESRF beamline ID10. *J. Synchrotron Radiat.* **21**, 594-599 (2014). <https://doi.org/10.1107/S1600577514003440>
- [15] K. Uesugi, M. Hoshino, A. Takeuchi, et al. Development of fast and high throughput tomography using CMOS image detector at SPring-8, proceedings of the Developments in X-

- ray tomography VIII. (SPIE, 2012). <https://doi.org/10.1117/12.929575>
- [16] H.J. Xu, Z.T. Zhao, J.H. He. SSRF in Full Commissioning. *Synchrotron Radiat. News* **21**, 20-23 (2008). doi: 10.1080/08940880802555376
  - [17] M.H. Jiang, X. Yang, H.J. Xu, et al. Shanghai Synchrotron Radiation Facility. *Chin. Sci. Bull.* **54**, 4171-4181 (2009). doi: 10.1007/s11434-009-0689-y
  - [18] H.J. Xu, Z.T. Zhao. Current status and progresses of SSRF project. *Nucl. Sci. Tech.* **19**, 1-6 (2008). [https://doi.org/10.1016/S1001-8042\(08\)60013-5](https://doi.org/10.1016/S1001-8042(08)60013-5)
  - [19] H.L. Xie, B. Deng, G.H. Du, et al. Methodology development and application of X-ray imaging beamline at SSRF. *Nucl. Sci. Tech.* **31**, 102 (2020). <https://doi.org/10.1007/s41365-020-00805-7>
  - [20] X.L. Ju, B. Deng, K. Li, et al. Calibrating the linearity between grayscale and element content for X-ray KES imaging of alloys. *Nucl. Sci. Tech.* **33**, 1 (2022). <https://doi.org/10.1007/s41365-022-00986-3>
  - [21] M.W. Xu, K. Li, Y.L. Xue, et al. Water refilling along vessels at initial stage of willow cuttage revealed by move contrast CT. *Front. Phys.* **11**, 1174387 (2023). <https://doi.org/10.3389/fphy.2023.1174387>
  - [22] F.X. Wang, K. Li, M.W. Xu, et al. Move contrast X-ray imaging and its applications. *Nucl. Instrum. Methods Phys. Res., Sect. A* **1055**, 168560 (2023). <https://doi.org/10.1016/j.nima.2023.168560>
  - [23] H.L. Xie, B. Deng, G.H. Du, et al. X-ray biomedical imaging beamline at SSRF. *J. Instrum.* **8**, C08003 (2013). doi: 10.1088/1748-0221/8/08/C08003
  - [24] R.C. Chen, P. Liu, T.Q. Xiao, et al. X-ray Imaging for Non-Destructive Microstructure Analysis at SSRF. *Adv. Mater.* **26**, 7688-7691 (2014). <https://doi.org/10.1002/adma.201402956>
  - [25] H.L. Xie, B. Deng, G.H. Du, et al. Latest advances of X-ray imaging and biomedical applications beamline at SSRF. *Nucl. Sci. Tech.* **26**, 020102 (2015). doi: 10.13538/j.1001-8042/nst.26.020102
  - [26] H.L. Xie, H.X. Luo, G.H. Du, et al. High-efficiency fast X-ray imaging detector development at SSRF. *J. Synchrotron Radiat.* **26**, 1631-1637 (2019). <https://doi.org/10.1107/S1600577519010075>
  - [27] Y.X. Zhang, H.L. Xie, G.H. Du, et al. Influence of scintillator's thickness on imaging quality of lens-coupled hard X-ray imaging detector. *Nucl. Tech.* **37**, 70102-70102 (2014). doi: 10.11889/j.0253-3219.2014.hjs.37.070102
  - [28] Y. Zhang, H.L. Xie, G.H. Du, et al. Fast reconstruction of X-ray dynamic micro-CT based on GPU parallel computing. *Nucl. Tech.* **44**, 060101 (2021). doi: 10.11889/j.0253-3219.2021.hjs.44.060101
  - [29] D. Fan, J.W. Huang, X.L. Zeng, et al. Simultaneous, single-pulse, synchrotron x-ray imaging and diffraction under gas gun loading. *Rev. Sci. Instrum.* **87**, 053903 (2016). <https://doi.org/10.1063/1.4950869>
  - [30] S. Moon. Novel insights into the dynamic structure of biodiesel and conventional fuel sprays from high-pressure diesel injectors. *Energy* **115**, 615-625 (2016). <https://doi.org/10.1016/j.energy.2016.09.062>
  - [31] S. De Iuliis, R. Dondè, I. Altman. Advancement in comprehending the evolution of nanooxides in flames using laser irradiation. *Chem. Phys. Lett.* **787**, 139213 (2022). <https://doi.org/10.1016/j.cplett.2021.139213>

- [32] M.L. Grünbein, R.L. Shoeman, R.B. Doak. Velocimetry of fast microscopic liquid jets by nanosecond dual-pulse laser illumination for megahertz X-ray free-electron lasers. *Opt. Express* **26**, 7190-7203 (2018). <https://doi.org/10.1364/OE.26.007190>
- [33] N.D. Parab. Investigating fracture mechanisms in opaque materials under dynamic loading using high-speed synchrotron X-ray imaging. *Advances in Experimental Impact Mechanics*. (Elsevier, 2022), pp. 285-314. <https://doi.org/10.1016/B978-0-12-823325-2.00008-X>
- [34] Z.J. Qiu, K. Li, H.L. Xie, et al. Study of 20 Hz high spatial-temporal resolution monochromatic X-ray dynamic micro-CT. *Nucl. Tech.* **46**, 070101 (2023). doi: 10.11889/j.0253-3219.2023.hjs.46.070101
- [35] H. Takano, M. Morikawa, S. Konishi, et al. Development of real-time x-ray microtomography system, proceedings of the Journal of Physics: conference series. (IOP Publishing, 2013). doi: 10.1088/1742-6596/463/1/012025
- [36] K. Li, Y.T. Gao, H.P. Zhang, et al. Efficient three-dimensional characterization of C/C composite reinforced with densely distributed fibers via X-ray phase-contrast microtomography. *Chin. Opt. Lett.* **19**, 073401 (2021). doi: 10.3788/COL202119.073401
- [37] K. Li, B. Deng, H.P. Zhang, et al. Comprehensive characterization of TSV etching performance with phase-contrast X-ray microtomography. *J. Synchrotron Radiat.* **27**, 1023-1032 (2020). <https://doi.org/10.1107/S1600577520005494>